



Effect of mixed anion layer on energy band, charge separation and photochemical properties of $(\text{BiO})_2\text{OHCl}$



Yifei Zhai¹, An Zhang¹, Fei Teng*, Yang Yang, Wenhao Gu, Weiyi Hao, Zailun Liu, Zhe Liu, Jinyu Yang, Yiran Teng

Jiangsu Engineering and Technology Research Center of Environmental Cleaning Materials (ECM), School of Environmental Science and Engineering, Nanjing University of Information Science & Technology, 219 Ningliu Road, Nanjing 210044, China

ARTICLE INFO

Keywords:

Mixed anion layer
Hydroxyl
Internal electric field
 $(\text{BiO})_2\text{OHCl}$

ABSTRACT

It is still a big challenge to reveal the correlation between crystal structure and properties. In this work, bismuth oxychloride ($(\text{BiO})_2\text{OHCl}$) is prepared by a simple precipitation method, and the effect of mixed anion layer on the photochemical properties is mainly investigated. The sample is characterized by polycrystalline X-ray powder diffraction (XRD), scanning electron microscope (SEM), infrared spectroscopy (IR), high-resolution transmission electron microscope (HRTEM), selection area electron diffusion (SAED), UV-visible diffuse reflectance spectra (UV-DRS), photoluminescence fluorescence (PL), etc. It is found that under ultraviolet light irradiation ($\lambda \leq 400$ nm), the photoactivity of $(\text{BiO})_2\text{OHCl}$ is 1.8 times higher than that of BiOCl for the degradation of MO, although $(\text{BiO})_2\text{OHCl}$ has a much lower BET area ($3.4 \text{ m}^2 \text{ g}^{-1}$) than BiOCl ($15.9 \text{ m}^2 \text{ g}^{-1}$). Comparing $(\text{BiO})_2\text{OHCl}$ with BiOCl , parts of Cl in the anion layer of BiOCl are replaced by hydroxyl. The mixed anion layer has shifted the energy bands down, compared with BiOCl . Because hydroxyl has a higher ability to attract electron than Cl, the insertion of OH^- has greatly increased the electron density of the anion layer of $(\text{BiO})_2\text{OHCl}$. Thus, the internal electric field (IEF) of $(\text{BiO})_2\text{OHCl}$ has been strengthened, which is firmly demonstrated by the photocurrent results. The strengthened IEF could favor for the separation and transfer of photogenerated charges, leading to an improved photoactivity. This study provides a new idea to develop the efficient photocatalysts through building mixed anion layer.

1. Introduction

Over the past decades, photocatalysis has attracted much attention for the promising applications in solving the severe problems of energy and environment [1–3]. Under light irradiation, photocatalysis technology can be used to decompose organic contaminants and split water [4–6]. Up to now, numerous photocatalysts have been developed, including oxides [7], sulfides [8], oxysalts [9], and polymers [10]. However, their practical applications are still limited by the low solar energy utilization and low quantum efficiency. Thus, it still remains a big challenge to develop efficient photocatalysts [11,12]. Recently, the *p*-block nonmetals-containing anions intercalation materials of bismuth oxide, like layer BiOX (X = halogen ions, CO_3^{2-} , SO_4^{2-} , etc.), have been researched intensively [13–15]. For example, Zhao et al. have reported that the internal electric field (IEF) of BiOCl benefits the charge separation and transfer [16]. Zhang et al. have also reported that layer $\text{Bi}_3\text{O}_4\text{Cl}$ has a high photocatalytic activity due to IEF [13]. In

addition, many hydroxyl-containing materials, e.g., $\text{ZnSn}(\text{OH})_6$ [17], $\text{In}(\text{OH})_3$ [18], $\text{CaSbO}(\text{OH})_3$ [19], etc. have also been reported to have the excellent photodegradation performances. Our group has also reported the photocatalytic properties of the hydroxyl-containing photocatalysts [20,21]. On base of the existing reports, the OH^- anions in the chemicals seem to easily capture the photogenerated holes to form hydroxyl radicals [20,21]. Herein, we have found that $(\text{BiO})_2\text{OHCl}$ shows an obviously higher activity than BiOCl . Moreover, $(\text{BiO})_2\text{OHCl}$ has the similar layer structure to BiOCl , in which parts of Cl^- in the anions layer of BiOCl are displaced by OH^- . It is desirable to reveal the influence of the mixed anion layer on photocatalytic properties.

In this work, BiOCl and $(\text{BiO})_2\text{OHCl}$ were synthesized by a hydrothermal and precipitation method, respectively. Herein, H_2O_2 was used as the source of OH^- to form $(\text{BiO})_2\text{OHCl}$. Their photocatalytic activities were investigated by the degradation of MO dye under ultraviolet light irradiation ($\lambda \leq 400$ nm). Moreover, the correlation of photochemical property with mixed anion layer has been studied mainly. To

* Corresponding author.

E-mail address: 001880@nuist.edu.cn (F. Teng).

¹ The first and second authors contribute equally in this work.

the best of our knowledge, $(\text{BiO})_2\text{OHCl}$ have not been reported as a photocatalyst before. In addition, the effect of the mixed anion layer on the photocatalytic properties of a semiconductor has not been reported. This finding suggests that the internal electric field of a layer structure can be optimized by introducing OH^- . Thus, we could develop the new, efficient photocatalysts through the introduction of hydroxyl.

2. Experimental section

2.1. Sample preparation

All reagents were of analytical grade, purchased from Beijing Chemical Reagents Industrial Company of China, and used without further purification.

2.1.1. $(\text{BiO})_2\text{OHCl}$

Typically, 0.466 g of Bi_2O_3 was added into 5 mL of H_2O and 5 mL H_2O_2 (30 vol%) under stirring. Subsequently, the slurry was transferred to autoclave and 0.58 g of NaCl was added into the slurry above. Then, the resulting slurry was aged at 40 °C for 4 h in water bath. After the autoclave was cooled to room temperature naturally, the solid was separated by centrifugation and washed with deionized water and ethanol for several times, respectively. Finally, the sample was dried at 60 °C for 6 h.

2.1.2. BiOCl

0.72 g of $\text{Bi}(\text{NO}_3)_3 \cdot 5\text{H}_2\text{O}$ was dissolved in 30 mL of glycol. Then, the NaCl solution (0.468 g) was added slowly into the above solution drop wise, which was kept stirring for 10 min. The resulting solution was transferred into a 40 mL Teflon-lined stainless steel autoclave and heated at 170 °C for 6 h. After the autoclave was cooled to room temperature naturally, the solid was separated by centrifugation and washed with deionized water and ethanol for several times, respectively. Finally, the sample was dried at 60 °C for 6 h.

2.2. Characterization

The crystal structures of the samples were determined by X-ray powder polycrystalline diffractometer (Rigaku D/max-2550VB), using graphite monochromatized Cu K_α radiation ($\lambda = 0.154$ nm), operating at 40 kV and 50 mA. The XRD patterns were obtained in the range of 20–80° (2θ) at a scanning rate of 4° min⁻¹. The samples were characterized on a scanning electron microscope (SEM, Hitachi SU-1510) with an acceleration voltage of 15 keV. The samples were coated with 5 nm thick gold layer before observations. The fine surface structures of the samples were determined by high-resolution transmission electron microscopy (HRTEM, JEOL JEM-2100F), equipped an electron diffraction (SAED) attachment with an acceleration voltage of 200 kV. UV-vis diffused reflectance spectra (UV-DRS) of the samples were obtained using a UV-vis spectrophotometer (UV-2550, Shimadzu, Japan). BaSO_4 was used as a reflectance standard in a UV-vis diffuse reflectance experiment. Nitrogen sorption isotherms were performed at 77 K and < 10⁻⁴ bar on a Micromeritics ASAP2010 gas adsorption analyzer. Each sample was degassed at 150 °C for 5 h before measurements. Surface area was calculated by the Brunauer–Emmett–Teller (BET) method.

2.3. Measurements of photoelectrochemistry properties

All the electrochemical measurements were carried out on a CHI 660D electrochemical working station at room temperature. For a standard three-electrode cell, a 0.5 M Na_2SO_4 aqueous solution was used as the electrolyte. ITO (with a geometric area of 2 cm²) was used as the current collector of working electrode for detecting photocurrent response, and Ni film (with a geometric area of 1 cm²) was used as the current collector of working electrode for testing EIS. Pt wire (diameter: 0.1 cm, length: 4 cm) and Hg/HgO (S.C.E) electrodes were used as the

counter and reference electrodes, respectively. To fabricate the working electrode, 80 wt% of active materials, 10 wt% of acetyleneblack (conductive agent) and 10 wt% of polyvinylidene fluoride (binder) were dispersed in 1-methyl-2-pyrrolidinone to form homogeneous slurry. Then the slurry was dotted on the ITO or Ni film, and dried for 24 h at room temperature. Electrochemical impedance spectroscopy (EIS) was performed from 0.1 Hz to 100 kHz at an open circuit potential of 0.3 V and an alternating current (AC) voltage amplitude of 5 mV. The photo electrodes were prepared by a dip-coating method and 0.5 M Na_2SO_4 aqueous solution was used as the electrolyte solution. Photoluminescence (PL) spectra were measured on a fluorescence spectrophotometer (Japan, Shimadzu RF-5301PC) with the 300 nm excitation wavelength of a Xe lamp as the excitation source.

Surface photovoltage (SPV) measurement system is consist of a monochromatic light source, a lock-in amplifier (SR830-DSP) with a light chopper (SR540), a photovoltaic cell and a computer. The monochromatic light is provided by a 500 W Xe lamp (CHFXQ500 W, Global Xenon Lamp Power) and a double-prism monochromator (Zolix SBP500). During the SPV measurement, the samples were test without further treatment. While the measurement of surface photovoltage was performed, the contact between the samples and the indium tin oxide (ITO) electrode was not ohmic. The construction of the photovoltaic cell is a sandwich like structure, which consist of steel timber, powder and ITO. We placed the powder on the steel timber electrode, then, the powder was pressed to obtain a film with ITO electrode.

2.4. Evaluation of photocatalytic activity

The photocatalytic activity of the sample was evaluated by the degradation of methyl orange (MO) aqueous solution and 2-nitrophenol aqueous solution under UV light ($\lambda \leq 400$ nm), using a 300 W Xe arc lamp (CEL-HXF 300) equipped with a cutoff filter ($\lambda > 400$ nm). The reaction system was placed in a sealed black box with the top opened, and the distance from reaction system to light source was maintained at 15 cm. The total irradiation power which impinged on sample was determined to be 0.1 W cm⁻². The powders (100 mg) were dispersed in 200 mL aqueous solution of MO (12.5 mg L⁻¹) or 2-nitrophenol (4.5 mg L⁻¹) in a Pyrex beaker at room temperature. Before lamp was turned on, the suspension was continuously stirred for 30 min in the dark to ensure the establishment of an adsorption–desorption equilibrium between the powders and MO. At a time interval, 3 mL of solution was collected by pipette, and subsequently centrifuged to remove the powders. The UV-vis spectrophotometer was used to determine the concentration of MO and 2-nitrophenol.

3. Results and discussion

3.1. Crystal structure and morphology of $(\text{BiO})_2\text{OHCl}$

Fig. 1(a) shows the X-ray diffraction (XRD) patterns of the samples. All the diffraction peaks are in good agreement with the standard card JCPDS 85-0861 and JCPDS 41-0708, confirming the formation of phase-pure BiOCl and $(\text{BiO})_2\text{OHCl}$, respectively. **Fig. 1(b,d)** shows that the Sillen-related BiOCl , with the unit cell parameters of $a = 3.89(1)$ Å, $b = 3.89(2)$ Å, $c = 7.37(7)$ Å, is composed of $[\text{Bi}_2\text{O}_2]^{2+}$ layers and Cl^- layers. In BiOCl , bismuth link to oxygen through five short and three long Bi–O bonds, the lone electron pair of Bi face toward the outsides of $[\text{Bi}_2\text{O}_2]^{2+}$ layer [22], and the bonds lengths of Bi–O(1) and Bi–O(2) are both 2.326 Å. **Fig. 1(c,e)**, shows that $(\text{BiO})_2\text{OHCl}$ also has a layer structure. Different from BiOCl , Cl^- and OH^- are both contained in the anion layer of $(\text{BiO})_2\text{OHCl}$. In $(\text{BiO})_2\text{OHCl}$, the bonds lengths are 2.280 Å and 2.393 Å for Bi–O(1) and Bi–O(2), respectively. Compared with BiOCl (72.509°), the O(1)–Bi–O(2) bond angle (72.294°) of $(\text{BiO})_2\text{OHCl}$ become smaller. Meanwhile, the distance between the cation layer and anion layer (1.328 Å) of BiOCl is smaller than that (1.518 Å) of $(\text{BiO})_2\text{OHCl}$. It is obvious that the bond lengths, bond

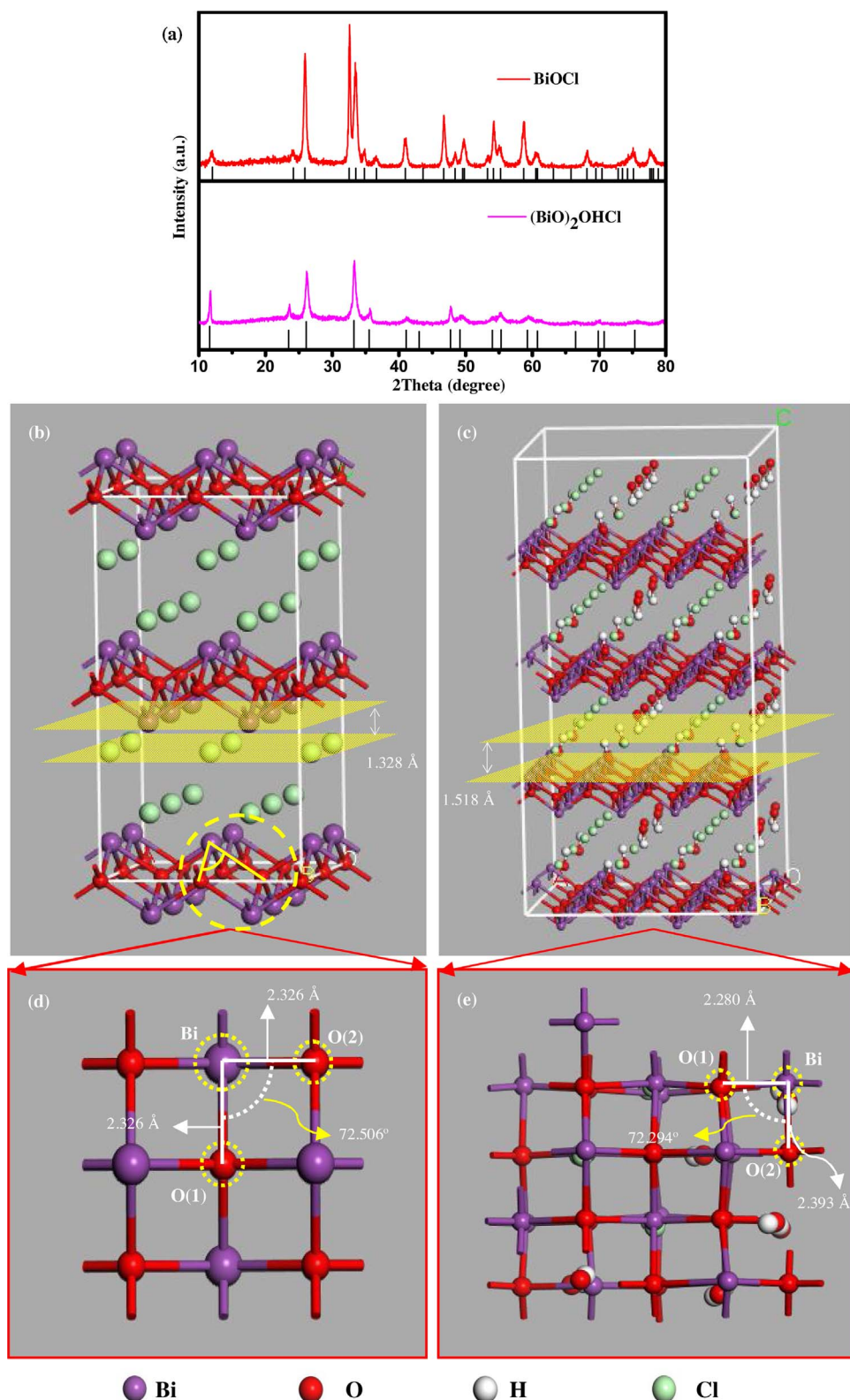


Fig. 1. XRD patterns (a) and crystal structures of (b,d) BiOCl and (c,e) (BiO)₂OHCl.

angles and layer spacing have all changed due to the introduction of hydroxyl in the anion layer. Besides, the samples are characterized by FT-IR spectroscopy, as shown in Fig. 2(a). The absorption bands at 1381 cm^{-1} could be assigned to the asymmetry and symmetric stretching vibrations of Bi-Cl bond [15]. The band at 540 cm^{-1} is recognized as Bi-O bonds [23]. The bands at 3416 and 1625 cm^{-1} are the stretching and flexural vibrations of O-H for adsorbed water

molecules, respectively [24]. Compared with BiOCl, the sharp, intense peaks at 3420 cm^{-1} (BiO)₂OHCl can be assigned to the stretching vibrations of O-H [25], suggesting the presence of hydroxyl in (BiO)₂OHCl.

XPS analysis was employed to explore surface chemical state and composition of the samples [26]. Observed from the survey spectra (Fig. 2b), the peaks of Bi, O and Cl are present for BiOCl and

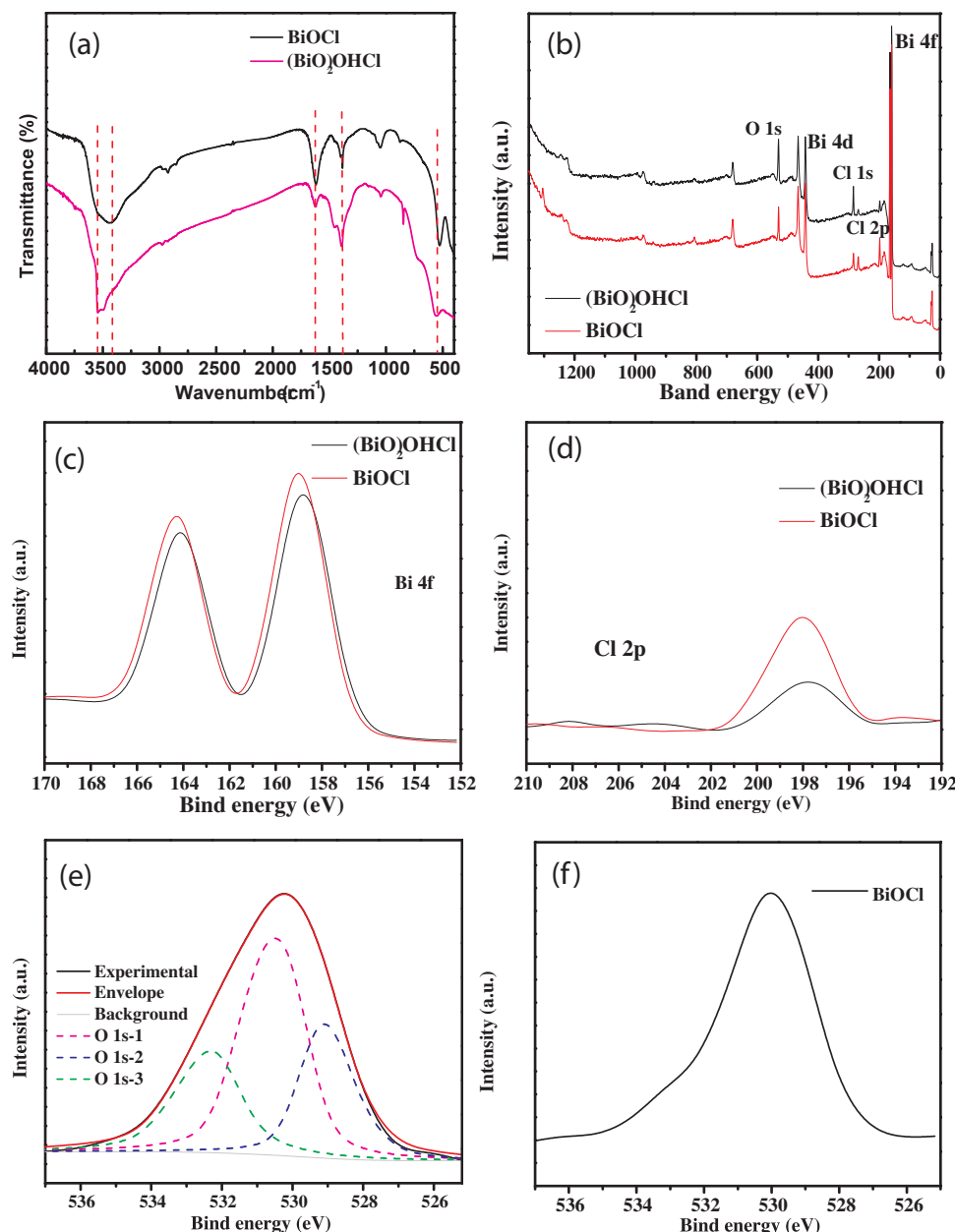


Fig. 2. (a)FT-IR spectra of BiOCl and $(\text{BiO})_2\text{OHCl}$; XPS spectra of the as-prepared samples: (b) Wide scan (survey); (c) Bi 4f; (d) Cl 2p; (e) O 1s of $(\text{BiO})_2\text{OHCl}$; (f) O 1s of BiOCl.

Table 1
Atomic concentration (atom%) of the BiOCl and $(\text{BiO})_2\text{OHCl}$.

Chemicals	Cl 2p	O 1s	Bi 4f
$(\text{BiO})_2\text{OHCl}$	6.08%	32.27%	12.52%
BiOCl	18.44%	24.32%	15.71%

$(\text{BiO})_2\text{OHCl}$. Fig. 2(c) displays two strong characteristic spin-orbit splitting peaks of Bi 4f at 159 eV and 164 eV, which are in accordance with the $\text{Bi } 4f_{7/2}$ and $\text{Bi } 4f_{5/2}$ signals, respectively [27]. In Fig. 2(d), the peaks at about 198 eV can be ascribed to $\text{Cl } 2p_{3/2}$ [28]. The high resolution O 1s spectrum of $(\text{BiO})_2\text{OHCl}$ can be seen in Fig. 2(e). The peak located at 530.2 eV is attributed to the lattice oxygen, and the other two peaks located at 529 eV and 532.2 eV can be assigned to the oxygen of $\text{Bi}-\text{O}$ and OH , respectively [29]. In Fig. 2(f), the peak at 530 eV presents the O 1s spectrum of BiOCl. Additionally, Table 1 summarizes the calculated atomic concentration of Cl, O and Bi. It is obvious that compared with BiOCl, the concentration of Cl decreased and the

concentration of O increased in $(\text{BiO})_2\text{OHCl}$, respectively.

Further, the particle morphologies are observed by scanning electron microscope (SEM) and high-resolution transmission electron microscope (HRTEM). Fig. S1(a) (seeing SI) shows that the BiOCl microspheres form, which are assembled by numerous nanosheets. Fig. S1(b) (seeing SI) shows that the $(\text{BiO})_2\text{OHCl}$ nanoparticles form. The interplanar lattice spacing are determined to be 0.27 nm, which can be indexed to the (110) facet of $(\text{BiO})_2\text{OHCl}$ (Fig. S1(c), seeing SI). Fig. S1(d) (seeing SI) shows the typical selected area electron diffraction patterns (SAED), revealing the single-crystal structure of $(\text{BiO})_2\text{OHCl}$. The clear diffraction spots can be indexed to the (110) and (200) facets of $(\text{BiO})_2\text{OHCl}$ along the [002] zone axis.

3.2. Optical property of $(\text{BiO})_2\text{OHCl}$

Fig. 3(a) displays the UV-vis diffuse reflection absorption spectra (UV-DRS) of the as-prepared BiOCl and $(\text{BiO})_2\text{OHCl}$ samples. As shown in Fig. 3(a), the absorption edge of BiOCl and $(\text{BiO})_2\text{OHCl}$ are determined to be at about 370 and 362 nm, respectively. The results

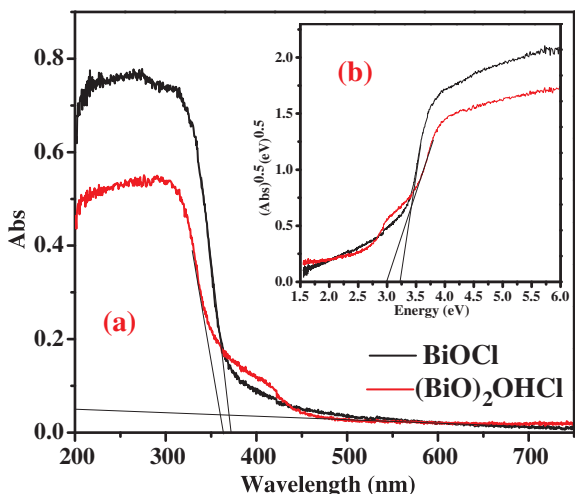


Fig. 3. UV-vis diffuse reflectance spectra (UV-DRS) (the inset of Tauc plot) of BiOCl and (BiO)₂OHCl.

confirmed that both BiOCl and (BiO)₂OHCl are UV light responsive photocatalysts. Besides, the band gap can be calculated by Eq. (1) as follows [30]:

$$ahv = A(hv - E_g)^n/2 \quad (1)$$

where α , h , v , E_g and A are absorption coefficient, Plank constant, light frequency, band gap energy and a constant, respectively. Amongst, n is determined by the optical transition type of a semiconductor ($n = 1$ for a direct transition semiconductor and $n = 4$ for an indirect transition semiconductor). According to the Tauc plot of $(ahv)^{0.5}$ vs. energy (hv) [31], the E_g values of both BiOCl and (BiO)₂OHCl are estimated to be 3.82 and 3.31 eV (Fig. 3(b)), respectively.

Furthermore, the conduction band (CB) and valence band (VB) potentials of BiOCl and (BiO)₂OHCl are calculated by the following equations [32]:

$$E_{VB} = \chi - E^c + 0.5E_g \quad (2)$$

$$E_{CB} = E_{VB} - E_g \quad (3)$$

where χ is the absolute electronegativity of a semiconductor, which is defined as the geometric average of the absolute electronegativity of constituent atoms, E^c is the energy of free electrons on the hydrogen scale (about 4.5 eV), and E_g is the band gap. For BiOCl, χ is calculated to be 6.63 eV. Consequently, E_{CB} and E_{VB} are estimated to be 0.22 and 4.04 eV, respectively. The χ of (BiO)₂OHCl is calculated to be 6.3748 eV, E_{CB} and E_{VB} are estimated to be 0.23 and 3.52 eV, respectively.

To investigate the effect of mixed anion layer on the energy bands, the energy band and electronic structures of BiOCl and (BiO)₂OHCl are calculated by using the *ab initio* density functional theory (DFT). Fig. 4(a) and (b) show the energy band structures of BiOCl and (BiO)₂OHCl, respectively. The highest occupied energy level has been taken as the valence band maximum (VBM), and the lowest unoccupied occupied state is the conduction band minimum (CBM). It can be found that for BiOCl, the VBM and CBM are located at 2.60 and 0 eV, respectively; and the band gap between VBM and CBM is about 2.60 eV. Besides, the band gap is about 2.49 eV for (BiO)₂OHCl (VBM = 2.53 eV, CBM = 0.04 eV). Obviously, the calculated values are smaller than the experimental values of the samples. It is worth noting that first-principles calculations generally underestimate the band gap value, because the improper treatment of open shell *d*-electrons of transition metal ions by gradient approximation approach (G-GA), and the approximate exchange energies cannot exactly cancel spurious Coulomb repulsion [33]. Simultaneously, both samples can be determined as the indirect band gap semiconductor. Zhao et al. [16]

have reported that compared with a direct band gap semiconductor, an indirect band gap semiconductor is not conducive to the light absorption, but it is favorable for the separation of photogenerated electron–hole pairs.

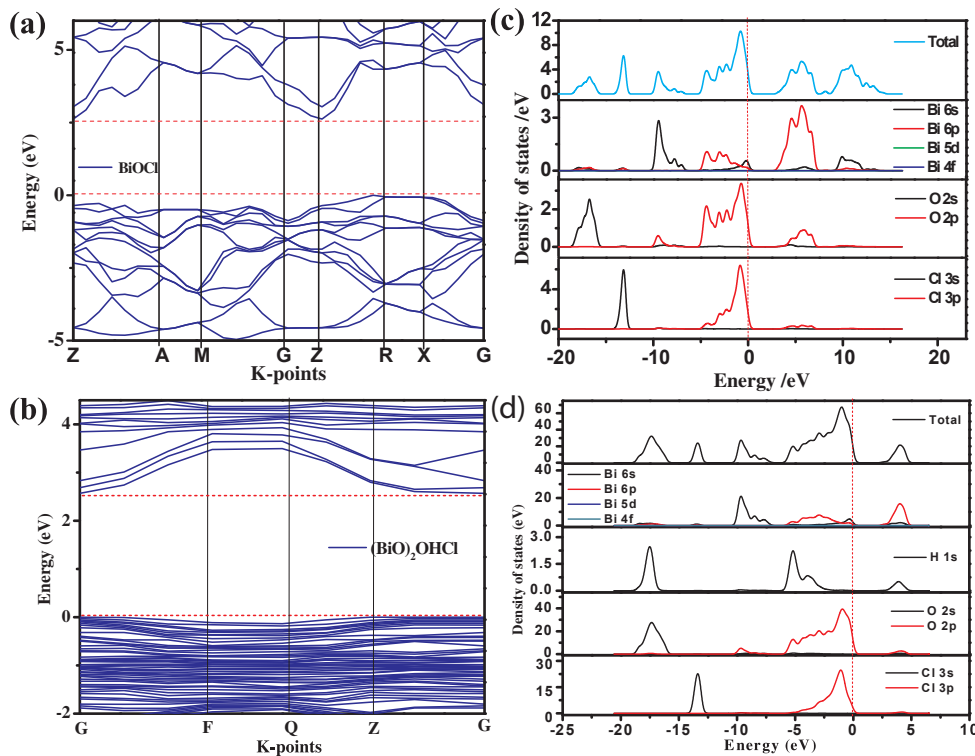
The density of states (DOS) calculations are carried out to reveal the detailed electronic structures of (BiO)₂OHCl and BiOCl. As shown in Fig. 4(c), the VB top of BiOCl is mainly composed of Bi 6s, O 2p and Cl 3p orbitals, while the CB bottom is mainly composed of Bi 6p and O 2p orbitals [16]. As shown in Fig. 4(d), the VB top of (BiO)₂OHCl mainly consists of Bi 6s, O 2p, and Cl 3p orbitals, and its CB bottom is mainly composed of Bi 6p and H 1s orbitals. The VB of BiOCl is mainly contributed by O and Cl, and its CB is mainly contributed by Bi and O. For (BiO)₂OHCl, O, Cl mainly contributed the VB, and Bi and H mainly contributed the CB. It is clear that the insertion of OH[−] has a significant influence on the energy band structure.

3.3. Photoelectrochemistry property of (BiO)₂OHCl

The photoluminescence emission spectrum (PL) can be used to characterize the recombination probability of photogenerated electrons and holes of a semiconductor [34,35]. Jing et al. [36] have reported that there are four photoluminescence (PL) processes. The main process is the photo-excited PL process (Process I), in which under irradiation, the electrons of VB can be excited to the CB with different energy levels to become different excited states, with simultaneous generation of holes in the VB. These excited electrons would easily recombine with the holes again. During the recombination process, a light radiation would dissipate, which results in a luminescence emission. In a band-band PL process (process II), the electrons transfer from the CB bottom to the VB top, with simultaneously releasing of energy as radiation. Process I and II can directly reflect the recombination of photo-induced carriers. The excitonic PL process (process III) is resultant from the surface defect, vacancy and surface states, which can bind electrons to form excitons. The process III cannot directly reflect the recombination of photo-induced carriers. Besides, the excited electrons at CB bottom can come back to VB directly or indirectly via non-radiative transitions (process IV). Therefore, the PL processes are complicate, and the recombination of electrons and holes can be reflected by process I and II, rather than by process III and IV. Summarily, the PL spectra can reflect the charge recombination rate at a certain extent. Wang et al. have reported that for BiOCl, the main emission peak located about 365 nm is attributed to the recombination of electrons from the bottom of the conduction band to the recombination center in the ground state [37]. In Fig. 5(a), the PL intensity of BiOCl is slightly lower than that of (BiO)₂OHCl at 362 nm. In general, a lower PL intensity means lower recombination probability of photogenerated carriers. But the peak intensity difference of BiOCl and (BiO)₂OHCl is too insignificant to reflect the recombination efficiency of the photogenerated carriers.

In order to further demonstrate the separation of the photo-generated carrier, the time-resolved fluorescence spectra was shown in Fig. S2 (SI). The decay profiles of (BiO)₂OHCl and BiOCl samples were fitted as a multi-exponential function. For the (BiO)₂OHCl sample, the three exponential constants (τ_1 , τ_2 and τ_3) are 0.419, 1.700 and 6.390 ns, respectively. The average lifetime (τ) was calculated to be 1.443 ns. For the BiOCl sample, the values of τ_1 , τ_2 and τ_3 are 0.348, 1.792 and 6.519 ns, respectively. The average lifetime was calculated to be 1.234 ns. The longer decay lifetime of (BiO)₂OHCl indicates that the photogenerated carriers has a lower recombination efficiency of (BiO)₂OHCl than BiOCl.

Besides, photocurrent spectrum can be used to reflect the separation and transfer efficiency of photogenerated electron-hole pairs [38]. Fig. 5(b) shows the photocurrent spectra of the (BiO)₂OHCl/ITO and BiOCl/ITO electrodes under UV light irradiation ($\lambda \leq 400$ nm). The photocurrent density of (BiO)₂OHCl/ITO is obviously higher than that of the latter, indicating that (BiO)₂OHCl has a higher charge transfer and separation efficiency. It could be expected that a high charge



transfer and separation efficiency favors for the photocatalytic activity [15].

The EIS spectra were provided as Fig. 5(c). In the inset of Fig. 5(c), the simulated equivalent electric circuit consists of solution resistance (R_s), charge transfer resistance (R_{ct}), constant phase element (CPE) accounting for electrical double-layer capacitance, and the open Warburg impedance (W_o) for ion diffusion. It is well known that in the high

frequency region, a smaller arc radius indicates a lower electrical resistance, which will favor for the electron transfer [39]. In Fig. 5(c), the arc radius of BiOCl sample is obviously larger than that of $(\text{BiO})_2\text{OHCl}$, indicating that the BiOCl sample has a higher electrical resistance than $(\text{BiO})_2\text{OHCl}$. The R_{ct} values were calculated to be 16.8Ω and 5.4Ω for BiOCl and $(\text{BiO})_2\text{OHCl}$, respectively. A high electron transfer rate of $(\text{BiO})_2\text{OHCl}$ favors for the charge separation.

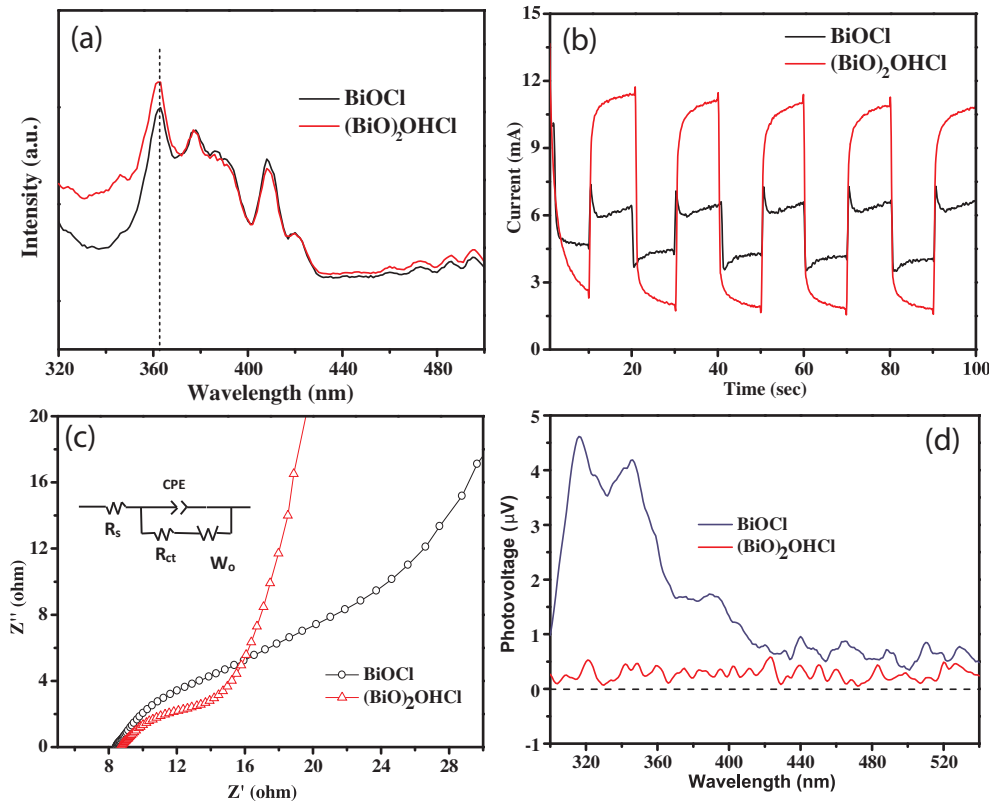


Fig. 5. (a) Photoluminescence spectra at an excitation wavelength of 300 nm; (b) Photocurrent under ultraviolet light irradiation ($\lambda \leq 400$ nm); (c) The electrochemical impedance spectra (EIS) Nyquist plots; (d) Surface photovoltage spectra (SPV) of the samples.

Further, Fig. 5(d) shows the surface photovoltage (SPV) spectra of the samples. For both $(\text{BiO})_2\text{OHCl}$ and BiOCl samples, all the responsive signals are positive in the range of 300 nm to 540 nm, meaning that the photo-induced holes mainly migrate from the bulk to the irradiation surface, but the photo-induced electrons mainly move from the surface to the bulk [40]. Moreover, the signal intensity of BiOCl is much stronger than that of $(\text{BiO})_2\text{OHCl}$. As we know, the formation of a SPV signal is determined by the ability of the light absorption and the transference of carriers in a semiconducting material [41]. In this case, a higher surface area of BiOCl ($15.9 \text{ m}^2 \text{ g}^{-1}$) than that of $(\text{BiO})_2\text{OHCl}$ ($3.4 \text{ m}^2 \text{ g}^{-1}$) may favor for the absorption of light, thus more photo-generated holes may migrate to and accumulate on the irradiation surfaces to form a higher SPV signal. Furthermore, Huang et al. have reported that the OH^- in the layer gap could trap the photogenerated holes which transfer in the layer structure under the irradiation [22]. Hence, a part of photogenerated holes which was trapped by OH^- were limited in the anion layer rather than transfer to the surface of the catalyst. This is also the reason for the lower SPV intensity of $(\text{BiO})_2\text{OHCl}$.

3.4. Photocatalytic activity of $(\text{BiO})_2\text{OHCl}$

Fig. 6(a) shows the degradation curves of MO dye over BiOCl and $(\text{BiO})_2\text{OHCl}$ under ultraviolet light irradiation ($\lambda \leq 400 \text{ nm}$). It can be obviously seen that $(\text{BiO})_2\text{OHCl}$ has a higher photocatalytic activity

than BiOCl for the degradation of MO (Fig. 6(a)). The degradation reaction of MO can be simplified by a pseudo-first-order kinetics (1) as follows.

$$\ln(C_0/C) = k_a t, \quad (4)$$

where C is the concentration of MO remained in solution after irradiation, and C_0 is the initial concentration of MO before irradiation. Fig. 6(b) shows their apparent reaction kinetic curves. The apparent rate constants (k_a) are 0.0077 min^{-1} and 0.0218 min^{-1} for BiOCl and $(\text{BiO})_2\text{OHCl}$, respectively. It is found that the photocatalytic reaction rate over $(\text{BiO})_2\text{OHCl}$ is 1.83 times higher than that over BiOCl . Generally, the activity of a photocatalyst can be affected by many factors, e.g., BET area, particle size, shape, charge separation and transfer efficiency, etc [42]. The BET areas of the BiOCl and $(\text{BiO})_2\text{OHCl}$ samples are measured to be $15.9 \text{ m}^2 \text{ g}^{-1}$ and $3.4 \text{ m}^2 \text{ g}^{-1}$, respectively. It seems that the BET area is not the crucial factor for the photoactivity. On base of the photocurrent results (Fig. 5(b)), we speculate that the charge separation and transfer efficiency may be the main affecting factor for the photoactivity. Moreover, their obviously different charge separation and transfer efficiencies may be relative to their different anion layers, as discussed in the latter section.

Besides, the trapping experiments have also been performed to explore the active oxidation species, in which ammonium oxalate, isopropyl alcohol (IPA) and benzoquinone (BQ) are used as the holes scavenger [43], the hydroxyl radical scavenger [44] and the reactive

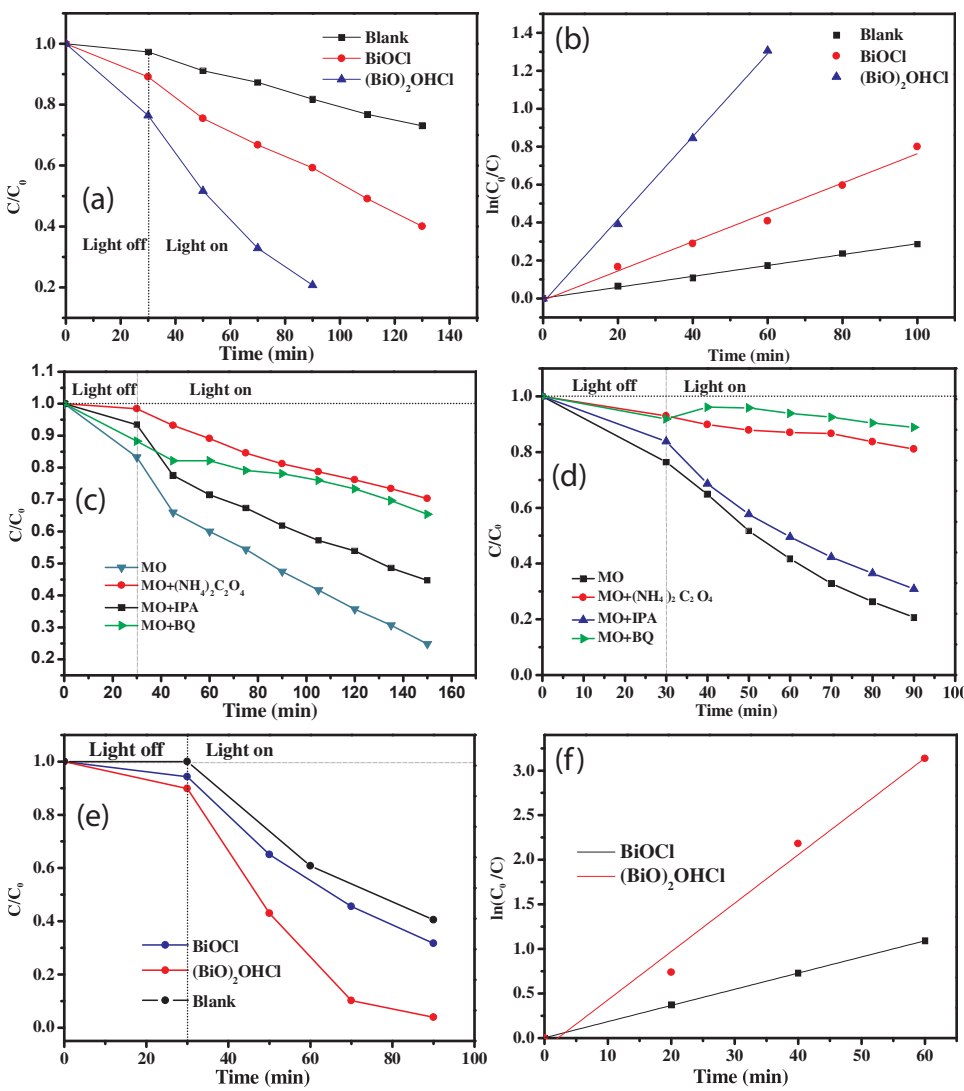


Fig. 6. (a) Degradation activities and (b) reaction kinetic curves of MO over BiOCl and $(\text{BiO})_2\text{OHCl}$ under ultraviolet light irradiation ($\lambda \leq 400 \text{ nm}$); The trapping experiments (c) BiOCl and (d) $(\text{BiO})_2\text{OHCl}$; (e) Degradation activities and (f) reaction kinetic curves of 2-nitrophenol over BiOCl and $(\text{BiO})_2\text{OHCl}$ under ultraviolet light irradiation ($\lambda \leq 400 \text{ nm}$).

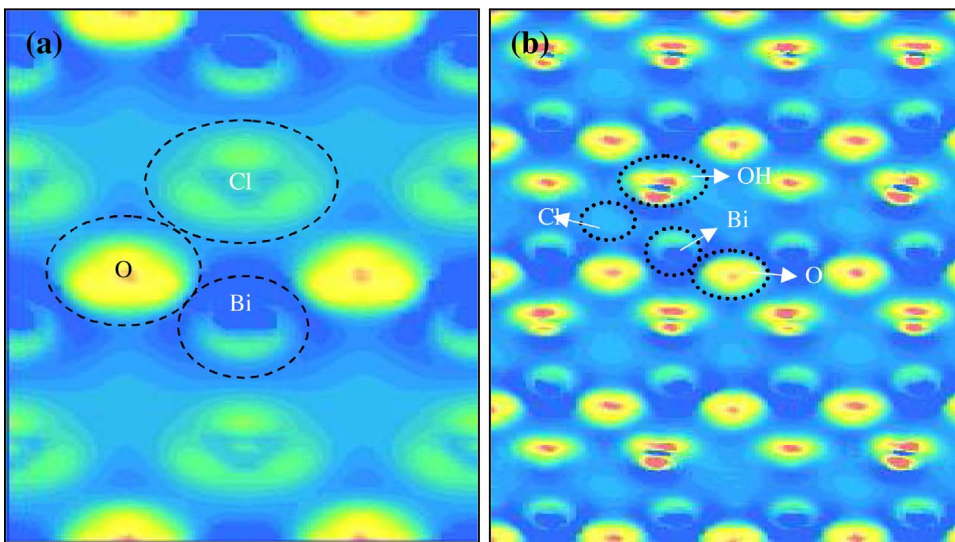


Fig. 7. Electron density contour plots: (a) BiOCl; (b) (BiO)₂OHCl.

oxygen ($\cdot\text{O}_2^-$) scavenger [28], respectively. Fig. 6(c) shows that for BiOCl, the degradation activity of MO decreases obviously while adding IPA, and the degradation activity is nearly inhibited while adding ammonium oxalate or BQ. The results above indicate that for BiOCl, $\cdot\text{O}_2^-$, holes and the hydroxyl radicals are the main active oxidative species in degradation process, but h^+ and $\cdot\text{O}_2^-$ play more important role than hydroxyls. Fig. 6(d) shows that the degradation activity of (BiO)₂OHCl is completely inhibited while adding ammonium oxalate or BQ, and is slightly affected by adding IPA. It is worth noting that for (BiO)₂OHCl, a slightly rise the curve may be due to a small desorption of MO while turn-on. For (BiO)₂OHCl, h^+ and $\cdot\text{O}_2^-$, as the active oxidative species, play a crucial role in the degradation of MO.

Furthermore, we have investigated the cycle stability of the BiOCl and (BiO)₂OHCl samples (Fig. S3(a,c), Seeing ESI). After three cycles, the degradation efficiency of the BiOCl and (BiO)₂OHCl decreased by about 4.6% and 15.1%, respectively. Fig. S3(b,d) (Seeing ESI) give the typical XRD patterns of BiOCl and (BiO)₂OHCl samples, which are collected after three cycles. All the XRD patterns have not changed after three cycles, confirming that both BiOCl and (BiO)₂OHCl have a high stability. Meanwhile, the SEM images (Fig. S3(e,f)) (Seeing ESI) also demonstrate that the samples have not changed after three cycles.

Herein, 2-nitrophenol without photosensitization was chosen to test the photocatalytic activities of BiOCl and (BiO)₂OHCl. Fig. 6(e) and (f) show the degradation curves and reaction kinetic curves of 2-nitrophenol under UV light irradiation ($\lambda \leq 400$ nm), respectively. After being irradiated for 60 min, 96% of 2-nitrophenol can be degraded by (BiO)₂OHCl; in contrast, only 75% of 2-nitrophenol can be degraded by BiOCl. Moreover, the apparent reaction rate constants (k_a) are 0.018 and 0.054 min^{-1} for BiOCl and (BiO)₂OHCl, respectively. It is obvious that 2-nitrophenol can be degraded by the photocatalysts.

3.5. Effect of mixed anion layer in (BiO)₂OHCl

Although (BiO)₂OHCl has a much lower BET area ($3.4 \text{ m}^2 \text{ g}^{-1}$) than BiOCl ($15.9 \text{ m}^2 \text{ g}^{-1}$), the photoactivity of (BiO)₂OHCl is 2.8 times higher than that of BiOCl. It seems that the BET area is not the crucial affecting factor for the photoactivity. It has been reported that the layer structure is beneficial for the charge separation and transfer because of the formed internal electric field (IEF) between cations layer and anions layer [22]. Because they have the similar layer structure (Fig. 1(b) and (c)), the effect of charge separation and transfer efficiency on the photocatalytic activity has been mainly considered [32,42]. It has been reported that in a layer structure, the non-uniform electron distribution between Cl anion layer and $[\text{Bi}_2\text{O}_2]^{2+}$ cation layer would polarize the

relative atoms and orbitals, leading to the formation of IEF. Fig. 7 shows the electron density distributions of BiOCl and (BiO)₂OHCl. In BiOCl, the electron density around O is obviously higher than that around Cl (Fig. 7(a)), and the electron density around OH^- is higher than that around Cl^- in (BiO)₂OHCl (Fig. 7(b)). Compared with BiOCl, the insertion of OH^- has greatly increased the electron density of the anion layer. As a result, the IEF of (BiO)₂OHCl could be enhanced, compared with BiOCl. The enhanced IEF could favor for the separation and transfer of photogenerated charges [45,46], which is firmly demonstrated by the photocurrent and EIS results (Fig. 5(b) and (c)).

Moreover, Huang et al. have reported that the OH^- in the layer gap could trap the photogenerated holes which transfer in the layer structure under the irradiation [22]. This rapid hole-trapping process makes the transfer of the photogenerated electrons easily, which can reduce the recombination of photogenerated carriers. As a result, (BiO)₂OHCl has a promoted photocatalytic activity because of the accelerated separation of photogenerated carriers. This work provides a new idea to develop the efficient photocatalysts through building mixed anion layer.

4. Conclusions

Bismuth oxychloride containing hydroxyl ((BiO)₂OHCl) can be prepared by a simple precipitation method. The photocatalytic activity of (BiO)₂OHCl is 1.8 times higher than BiOCl, although the BET area of former is much smaller than that of the latter. Its higher activity has been mainly attributed to the part substitution of hydroxyl for Cl. Due to the higher electron attraction ability of OH than Cl, the insertion of OH^- has greatly increased the electron density of the anion layer, thus improving the IEF of (BiO)₂OHCl that favors for the charge separation and transfer. We could develop the efficient photocatalysts through building mixed anion layer.

Acknowledgments

This work is financially supported by National Science Foundation of China (21377060), Scientific Research Foundation for the Returned Overseas Chinese Scholars of State Education Ministry (2013S002), the Key Project of Environmental Protection Program of Jiangsu (2013005), Postgraduate Research & Practice Innovation Program of Jiangsu Province (SJZZ16_0153) Six Talent Climax Foundation of Jiangsu (20100292), “333” Outstanding Youth Scientist Foundation of Jiangsu (20112015), the Project Funded by the Science and Technology Infrastructure Program of Jiangsu (BM201380277), Jiangsu Science

Foundation of China (BK2012862).

Appendix A. Supplementary data

Supplementary data associated with this article can be found, in the online version, at <http://dx.doi.org/10.1016/j.apcatb.2017.10.055>.

References

- [1] H. Tong, S. Ouyang, Y. Bi, N. Umezawa, M. Oshikiri, J. Ye, *Adv. Mater.* 24 (2012) 229–251.
- [2] M.W. Kanan, D.G. Nocera, *Science* 321 (2008) 1072–1075.
- [3] A.L. Linsebigler, G. Lu, J.T. Yates, *Chem. Rev.* 95 (1995) 735–758.
- [4] J. Wang, Y. Yu, L. Zhang, *Appl. Catal. B: Environ.* 136–137 (2013) 112–121.
- [5] S.S. Ma, T. Hisatomi, K. Maeda, Y. Moriya, K. Domen, *J. Am. Chem. Soc.* 134 (2012) 19993–19996.
- [6] S. Zhang, H. Gao, X. Liu, Y. Huang, X. Xu, N.S. Alharbi, T. Hayat, J. Li, *ACS Appl. Mater. Interface* 8 (2016) 35138–35149.
- [7] M. Muruganandham, R. Amutha, G.-J. Lee, S.-H. Hsieh, J.J. Wu, M. Sillanpää, *J. Phys. Chem. C* 116 (2012) 12906–12915.
- [8] L. Huang, X. Wang, J. Yang, G. Liu, J. Han, C. Li, *J. Phys. Chem. C* 117 (2013) 11584–11591.
- [9] S. Li, S. Liu, S. Liu, Y. Liu, Q. Tang, Z. Shi, S. Ouyang, J. Ye, *J. Am. Chem. Soc.* 134 (2012) 19716–19721.
- [10] T. Wen, D.X. Zhang, J. Zhang, *Inorg. Chem.* 52 (2013) 12–14.
- [11] M. Dong, Q. Lin, H. Sun, D. Chen, T. Zhang, Q. Wu, S. Li, *Cryst. Growth Des.* 11 (2011) 5002–5009.
- [12] D. Li, H. Haneda, N.K. Labhsetwar, S. Hishita, N. Ohashi, *Chem. Phys. Lett.* 401 (2005) 579–584.
- [13] J. Li, L. Zhang, Y. Li, Y. Yu, *Nanoscale* 6 (2014) 167–171.
- [14] Y. Zheng, F. Duan, M. Chen, Y. Xie, *J. Mol. Catal. A—Chem.* 317 (2010) 34–40.
- [15] J. Xu, Y. Teng, F. Teng, *Sci. Rep.-UK* 6 (2016) 32457–32466.
- [16] Z.Y. Zhao, W.W. Dai, *Inorg. Chem.* 53 (2014) 13001–13011.
- [17] X. Fu, X. Wang, Z. Ding, D.Y.C. Leung, Z. Zhang, J. Long, W. Zhang, Z. Li, X. Fu, *Appl. Catal. B: Environ.* 91 (2009) 67–72.
- [18] T. Yan, J. Long, X. Shi, D. Wang, Z. Li, X. Wang, *Environ. Sci. Technol.* 44 (2010) 1380–1385.
- [19] M. Sun, D. Li, Y. Zheng, W. Zhang, Y. Shao, Y. Chen, W. Li, X. Fu, *Environ. Sci. Technol.* 43 (2009) 7877–7882.
- [20] H. Tian, F. Teng, J. Xu, S. Lou, N. Li, Y. Zhao, M. Chen, *Sci. Rep.—UK* 5 (2015) 7770–7779.
- [21] Y. Zhao, F. Teng, J. Xu, Z. Liu, Y. Yang, Q. Zhang, W. Yao, *RSC Adv.* 5 (2015) 100934–100942.
- [22] H. Huang, Y. He, Z. Lin, L. Kang, Y. Zhang, *J. Phys. Chem. C* 117 (2013) 22986–22994.
- [23] D. Wu, S. Yue, W. Wang, T. An, G. Li, H.Y. Yip, H. Zhao, P.K. Wong, *Appl. Catal. B: Environ.* 192 (2016) 35–45.
- [24] J.-M. Song, C.-J. Mao, H.-L. Niu, Y.-H. Shen, S.-Y. Zhang, *CrystEngComm* 12 (2010) 3875–3881.
- [25] H. Huang, Y. He, X. Li, M. Li, C. Zeng, F. Dong, X. Du, T. Zhang, Y. Zhang, *J. Mater. Chem. A* 3 (2015) 24547–24556.
- [26] S. Zhang, H. Yang, H. Gao, R. Cao, J. Huang, X. Xu, *ACS Appl. Mater. Interfaces* 9 (2017) 23635–23646.
- [27] C.Y. Wang, X. Zhang, X.N. Song, W.K. Wang, H.Q. Yu, *ACS Appl. Mater. Interfaces* 8 (2016) 5320–5326.
- [28] Y. Yang, F. Teng, Y. Kan, L. Yang, Z. Liu, W. Gu, A. Zhang, W. Hao, Y. Teng, *Appl. Catal. B: Environ.* 205 (2017) 412–420.
- [29] J. Zhang, H. Gu, X. Yang, M. Chen, Z. Yang, W. Zhang, *RSC Adv.* 5 (2015) 8537–8543.
- [30] Y. Ohko, K. Hashimoto, A. Fujishima, *J. Phys. Chem. A* 101 (1997) 8057–8062.
- [31] N. Sahai, *Environ. Sci. Technol.* 36 (2002) 445–452.
- [32] X. Zhang, L. Zhang, T. Xie, D. Wang, *J. Phys. Chem. C* 113 (2009) 7371–7378.
- [33] R. Christensen, H.A. Hansen, T. Vegge, *Catal. Sci. Technol.* 5 (2015) 4946–4949.
- [34] G. Tian, Y. Chen, J. Zhou, C. Tian, R. Li, C. Wang, H. Fu, *CrystEngComm* 16 (2014) 842–849.
- [35] K. Wang, J. Xu, X. Hua, N. Li, M. Chen, F. Teng, Y. Zhu, W. Yao, *J. Mol. Catal. A: Chem.* 393 (2014) 302–308.
- [36] L. Jing, Y. Qu, B. Wang, S. Li, B. Jiang, L. Yang, W. Fu, H. Fu, J. Sun, *J. Sol. Energy Mater. Sol. C* 90 (2006) 1773–1787.
- [37] L. Zhang, W. Wang, D. Jiang, E. Gao, S. Sun, *Nano Res.* 8 (2014) 821–831.
- [38] Y. Hou, A.B. Laursen, J. Zhang, G. Zhang, Y. Zhu, X. Wang, S. Dahl, I. Chorkendorff, *Angew. Chem.* 52 (2013) 3621–3625.
- [39] H. Huang, X. Li, J. Wang, F. Dong, P.K. Chu, T. Zhang, Y. Zhang, *ACS Catal.* 5 (2015) 4094–4103.
- [40] P. Wang, T.F. Xie, H.Y. Li, L. Peng, Y. Zhang, T.S. Wu, S. Pang, Y.F. Zhao, D.J. Wang, *Chem. Eur.* 15 (2009) 4366–4372.
- [41] H. Fan, T. Jiang, H. Li, D. Wang, L. Wang, J. Zhai, D. He, P. Wang, T. Xie, *J. Phys. Chem. C* 116 (2012) 2425–2430.
- [42] Y. Lv, Y. Liu, Y. Zhu, Y. Zhu, *J. Mater. Chem. A* 2 (2014) 1174–1182.
- [43] Z. Shan, W. Wang, X. Lin, H. Ding, F. Huang, *J. Solid State Chem.* 181 (2008) 1361–1366.
- [44] R. Palominos, J. Freer, M.A. Mondaca, H.D. Mansilla, *J. Photochem. Photobiol. A* 193 (2008) 139–145.
- [45] K. Zhang, C. Liu, F. Huang, C. Zheng, W. Wang, *Appl. Catal. B: Environ.* 68 (2006) 125–129.
- [46] X. Lin, T. Huang, F. Huang, W. Wang, J. Shi, *J. Phys. Chem. B* 110 (2006) 24629–24634.